

Tunable layered-magnetism-assisted magneto-Raman effect in a two-dimensional magnet CrI_3

Wencan Jin,^{1,*} Zhipeng Ye,² Xiangpeng Luo,¹ Bowen Yang,³ Gaihua Ye,² Fangzhou Yin,³ Hyun Ho Kim,^{3,†} Laura Rojas,² Shangjie Tian,⁴ Yang Fu,⁴ Shaohua Yan,⁴ Hechang Lei,⁴ Kai Sun,¹ Adam W. Tsen,³ Rui He,^{2,‡} and Liuyan Zhao^{1,§}

¹*Department of Physics, University of Michigan,
450 Church Street, Ann Arbor, Michigan 48109, USA*

²*Department of Electrical and Computer Engineering,
910 Boston Avenue, Texas Tech University, Lubbock, Texas 79409, USA*

³*Institute for Quantum Computing, Department of Chemistry,
and Department of Physics and Astronomy, University of Waterloo,
Waterloo, 200 University Ave W, Ontario N2L 3G1, Canada*

⁴*Department of Physics and Beijing Key Laboratory of
Opto-electronic Functional Materials & Micro-nano Devices,
Renmin University of China, Beijing 100872 China*

Abstract

We use a combination of polarized Raman spectroscopy experiment and model magnetism-phonon coupling calculations to study the rich magneto-Raman effect in the two-dimensional (2D) magnet CrI_3 . We reveal a novel layered-magnetism-assisted phonon scattering mechanism below the magnetic onset temperature, whose Raman excitation breaks time-reversal symmetry, has an antisymmetric Raman tensor, and follows the magnetic phase transitions across critical magnetic fields, on top of the presence of the conventional phonon scattering with symmetric Raman tensors in N -layer CrI_3 . We resolve in data and by calculations that the 1st-order A_g phonon of monolayer splits into a N -fold multiplet in N -layer CrI_3 due to the interlayer coupling ($N \geq 2$) and that the phonons with the multiple show distinct magnetic field dependence because of their different layered-magnetism-phonon coupling. We further find that such a layered-magnetism-phonon coupled Raman scattering mechanism extends beyond 1st-order to higher-order multi-phonon scattering processes. Our results on magneto-Raman effect of the 1st-order phonons in the multiplet and the higher-order multi-phonons in N -layer CrI_3 demonstrate the rich and strong behavior of emergent magneto-optical effects in 2D magnets and underlines the unique opportunities of new spin-phonon physics in van der Waals layered magnets.

* current affiliation: Department of Physics, Auburn University, 380 Duncan Drive, Auburn, AL 36849, USA

† current affiliation: School of Materials Science and Engineering, Kumoh National Institute of Technology, Gumi,

Gyeongbuk 39177, Korea

‡ rui.he@ttu.edu

§ lyzhao@umich.edu

Two-dimensional (2D) CrI₃ of few-layer form features a layered-antiferromagnetic (AFM) order where the spins align along the out-of-plane direction ferromagnetically within each layer and antiferromagnetically between adjacent layers [1–5]. It undergoes a layered-AFM to FM phase transition upon applying a moderate magnetic field [1–7], or electric field [8–10], or electrostatic doping [11], or hydrostatic pressure [12, 13]. The strong coupling between spin and charge degrees of freedom in 2D CrI₃ allows magneto-optical effects manifested in a variety of ways including large magneto-optical Kerr effect [5] and magnetic circular dichroism [8–13], spontaneous helical photoluminescence [14], giant nonreciprocal second harmonic generation [15], and anomalous magneto-optical Raman effect [7, 16–19]. All of these magneto-optical effects can be tuned across the layered-AFM to FM phase transition, making 2D CrI₃ a promising candidate for applications in magnetic sensors, optical modulation, and data storage.

Among all magneto-optical effects in CrI₃, magneto-optical Raman effect is of particular interest for two reasons. First, among all known magnets, the largest magnetism-induced optical rotation is observed for the linearly polarized, inelastically scattered light off the A_g phonon mode ($\sim 129 \text{ cm}^{-1}$) in the FM phase of CrI₃ [16]. Second, different phonon modes exhibit distinct magneto-optical behavior that the A_g mode emerges whereas its neighboring antisymmetric mode ($\sim 127 \text{ cm}^{-1}$) disappears in the linear crossed polarization channel across the layered-AFM to FM transition [7, 16–18]. However, the physical origin of magneto-optical Raman effect remains elusive with diverse proposals ranging from Davydov-split for bilayer CrI₃ [16, 18], zone-folded phonon for few-layer CrI₃ [17], and coupled magnetism-phonon scattering for bulk CrI₃ [7], none of which can be trivially generalized to explain CrI₃ of arbitrary thickness.

In this work, we carefully examine the magneto-optical Raman effect for N -layer CrI₃ ($N = 1 - 4$) by performing polarization, temperature, and magnetic field dependent micro-Raman spectroscopy measurements and unambiguously identify the layered-magnetism-assisted phonon scattering as the origin applicable for CrI₃ of any thickness. N -layer CrI₃ flakes were exfoliated from high-quality CrI₃ single crystals, sandwiched between hexagonal boron nitride (hBN) thin flakes, and then placed onto SiO₂/Si substrates inside a high-purity (> 99.999%) nitrogen-filled glove-box. Micro-Raman spectroscopy measurements in the backscattering geometry were carried out with a 633 nm excitation laser resonant with the charge-transfer transition [14], inside a vacuum cryostat at a base pressure lower than 7×10^{-7} mbar, and under an out-of-plane magnetic field (B_{\perp}) up to 2.2 T.

We start with resolving in N -layer CrI₃ the interlayer coupling-induced split of the A_g mode

of monolayer CrI₃ [20, 21]. Figure 1A shows Raman spectra in both parallel and crossed linear polarization channels taken at $T = 10$ K and $B_{\perp} = 0$ T on 1 – 4L CrI₃ (see full-range spectra in both channels and comparison to off-resonance 532 nm excitations in *SM* Section I, Figures S1 and S2, respectively). It has been established for CrI₃ that the modes in the crossed channel in Fig. 1A correspond to antisymmetric Raman tensor (R_{AS}) whereas those in the parallel channel are for symmetric Raman tensor of A_g symmetry (R_S) [19]. We highlight three key observations that have not been reported in previous work [7, 16–19, 22, 23] and summarize them in Fig. 1B with fitted mode frequencies vs. N . First, the number of modes increases proportional to the number of layers (with an exception for $N = 3$ that is explained in *SM* Section II). Second, the highest frequency remains constant while the lowest frequency decreases with increasing N , leading to a greater frequency separation between them. Third, the parallel and crossed channels show modes of the same frequencies for odd N whereas they select modes with distinct frequencies for even N . To interpret the A_g mode splitting, we take a simple linear chain model of N -layer CrI₃, as introduced in few-layer transition metal dichalcogenides [24–27],

$$H = H_0 + \frac{1}{2} \sum_{i=2}^N k(u_{i-1} - u_i)^2, \text{ with } H_0 = \sum_{i=1}^N (\frac{1}{2} m \dot{u}_i^2 + \frac{1}{2} k_0 u_i^2)$$

where H_0 represents the original A_g mode at frequency $\omega_0 = \sqrt{k_0/m}$ within individual layers, u_i represents the displacement field in the i^{th} layer, and k stands for the coupling constant between adjacent layers, equivalent to a coupling frequency $\omega = \sqrt{k/m}$. Diagonalizing H leads to N non-degenerate eigenfrequencies $\Omega_i(\omega_0, \omega)$ and their corresponding eigenmodes $\vec{U}_i (i = 1, 2, \dots, N)$ (*i.e.*, Davydov-splitting), with $i = 1$ being the highest frequency mode and $i = N$ being the lowest frequency mode. By choosing $\omega_0 = 129.10 \pm 0.10 \text{ cm}^{-1}$ and $\omega = 15.98 \pm 0.55 \text{ cm}^{-1}$, the calculated frequencies Ω_i (solid lines with open diamonds) match well with all the experimental values (ruby filled squares and royal filled circles), as highlighted by the fan-diagram in Fig 1B. See detailed calculations of Ω_i and \vec{U}_i in *SM* Section II, Table S1 and S2.

Because N -layer CrI₃ is structurally centrosymmetric, its N calculated eigenmodes have alternating parities, with the highest-frequency mode always parity-even as a result of equal, in-phase atomic displacement between layers (*i.e.*, $\vec{U}_1 = (1, 1, \dots, 1)/\sqrt{N}$). In the parallel channel where only modes with even parity and symmetric Raman tensor R_S can be detected, we expect to see every other mode starting with the highest frequency one ($i = 1, 3, 5, \dots$). This expectation is indeed consistent with our data that U_1 for $N = 1$ and 2 and $U_{1,3}$ for $N = 3$ and 4 are observed in the linear parallel channel in Fig. 1A and 1B. In contrary to the structure of N -layer CrI₃, the layered-AFM order is centrosymmetric for odd N and non-centrosymmetric for even N . Therefore, it should

couple to parity-even phonon modes for odd N and parity-odd phonon modes for even N to make the coupled layered-AFM-phonon entity parity-even and thus Raman-active. Due to the broken time-reversal symmetry from the magnetism, this layer-AFM-assisted phonon scattering corresponds to anti-symmetric Raman tensor R_{AS} and can only appear in the linear crossed channel. We anticipate observing in the crossed channel every other mode from the lowest-frequency one ($i = N, N - 2, N - 4, \dots$), because \vec{U}_N always has the same parity as the layered-AFM for any N . The result in Fig. 1A and 1B corroborates with this prediction that U_1 for $N = 1$, U_2 for $N = 2$, $U_{3,1}$ for $N = 3$, and $U_{4,2}$ for $N = 4$ are present in the linear crossed channel. The coupling efficiency between a phonon mode and the layered-AFM order can be evaluated by the projection $\vec{U}_i \cdot \vec{M}$ of the eigenmode vector \vec{U}_i onto the pseudo-vector (*i.e.*, axial vector) for the layered-AFM $\vec{M} = (1, -1, \dots, (-1)^{N-1})$ with +1 for spin up and -1 for spin down in a single layer. In particular, for any $N > 1$, the lowest-frequency mode \vec{U}_N features out-of-phase atomic displacement between adjacent layers and matches best the pattern of alternating spin orientations in the layered-AFM state (Fig. 1C), yielding the strongest coupling strength ($\vec{U}_i \cdot \vec{M}$) and thus the most intense signal among the modes in the linear crossed channel (Fig. 1A). See the computed $\vec{U}_i \cdot \vec{M}$ in the layered-AFM state of 1-4L CrI₃ in SM, Table S3.

So far we have established the physical origin of the N -fold multiplet for N -layer CrI₃ as a combined effect of Davydov-splitting and layered-AFM-phonon coupling, leading to the conventional phonons of R_S in the linear parallel channel [24–27] and the layered-AFM-coupled phonons of R_{AS} in the linear crossed channel [7, 19]. We note that a magnetism-induced symmetric E_g phonon mode splitting was previously reported in 2D Cr₂Ge₂Te₆ [28]. Here, the structural and magnetic nature of modes in the linear parallel and crossed channel, respectively, is further supported by their distinct temperature dependence of modes in these two channels. Taking 2L CrI₃ as an example, the linear crossed channel signal emerges below the magnetic transition temperature $T_C = 45$ K whereas the parallel channel signal is present above T_C and only increases slowly below T_C , as illustrated by representative spectra taken at 70 K, 40 K, and 10 K in Fig. 2A. Such a behavior extends beyond the 1st-order phonons (Fig. 2A, left) to the 2nd, and 3rd-order ones (Fig. 2A, middle and right, respectively). For all three orders, the temperature dependence of integrated intensity (I. I.) in the linear crossed channel fits well with an order parameter-like function $I_0 + I\sqrt{T_C - T}$ (royal curves in Fig. 2B), in contrast to those in the linear parallel channel following a smooth anharmonic decay behavior [29] (ruby curves in Fig. 2B). As pictorially summarized in Fig. 2C, we propose that a multi-phonon process [30, 31] leads to conventional 1st, 2nd, and 3rd-

order phonon modes (ruby) in the linear parallel channel, and its coupling with the layered-AFM order results in the magnetic counterparts (royal) in the linear crossed channel.

We then proceed to explore the magnetic field dependence of the layered-magnetism-assisted phonon modes in N -layer CrI_3 . From now on, we chose circularly polarized light to perform Raman measurements for preventing any artifacts from Faraday rotation of light passing through optical components in stray magnetic field. In this work, we focus on two representative thicknesses, 2L and 4L CrI_3 , having one and two critical magnetic transitions, respectively. We note that the mechanism described below is applicable for arbitrary N -layer CrI_3 .

The 2L CrI_3 undergoes a layered-AFM to FM transition at a critical magnetic field $B_c = \pm 0.6$ T [5]. Figure 3A presents Raman spectra of 1st-order modes taken at $B_\perp = 0$ T and ± 1.4 T, below and above B_c , respectively, at 10 K in both LL and RR channels, where LL(RR) stands for the polarization channel in which the incident and scattered light is left(right)-hand circularly polarized. At 0 T, both modes (U_1 and U_2) of 2L CrI_3 are present in Raman spectra that are identical in LL and RR channels. At ± 1.4 T, only the high-frequency mode (U_1) survives, and it shows giant circular dichroism of $\pm 78\%$ ($\frac{I_{LL} - I_{RR}}{I_{LL} + I_{RR}}$). See the comparison of selection rules between linear and circular polarization bases for 2L CrI_3 in SM, Table S5. The magnetic field dependence of U_2 integrated intensity clearly shows its disappearance at B_c , whereas that of U_1 increases (decreases) abruptly in the LL (RR) channel at B_c , as shown in Fig. 3B. Figure 3E and 3F show the magnetic field dependence of the 2nd and 3rd-order modes of 2L CrI_3 . Both of them mimic the magnetic field dependence of U_1 with a reduction of circular dichroism above B_c , $\pm 71\%$ for the 2nd-order and $\pm 50\%$ for the 3rd-order. This observation suggests the participation of U_1 in the 2nd, and 3rd-order multi-phonon process.

We refer to the layered-magnetism-phonon coupling that we have developed above to understand the magnetic field dependence of the two 1st-order modes (U_1 and U_2) in 2L CrI_3 . For each mode \vec{U}_i , its Raman tensor R^i is composed of the conventional structural (R_S^i) and the novel layered-magnetism-assisted magnetic (R_{AS}^i) contributions, *i.e.*, $R^i = R_S^i + \lambda_i R_{AS}^i$, where R_S^i is magnetic field independent and is only present for parity-even modes, $R_{AS}^i \propto \vec{U}_i \cdot \vec{M}$ reflects the magnetic origin and selects the zero-momentum component, and λ_i is ratio of the magnetic to structural contribution for the i^{th} mode that depends on microscopic parameters such as spin-orbit-coupling. Here, \vec{M} changes from (1,-1) to ($\pm 1, \pm 1$) across the layered-AFM to FM transition at $B_c = \pm 0.6$ T with the fully polarized FM spin moments pointing upwards/downwards. Specifically, for the

parity-even high-frequency mode of $\vec{U}_1 = \frac{1}{\sqrt{2}}(1, 1)$, $R_S^1 = \begin{pmatrix} a_1 & \\ & a_1 \end{pmatrix}$ at all magnetic fields and $R_{AS}^1 = \vec{U}_i \cdot \vec{M} \begin{pmatrix} & -a_1 i \\ +a_1 i & \end{pmatrix} = 0$ below B_c and $\begin{pmatrix} & \mp\sqrt{2}a_1 i \\ \pm\sqrt{2}a_1 i & \end{pmatrix}$ above B_c (Fig. 3C, top and bottom), whereas for the parity-odd low-frequency mode of $\vec{U}_2 = \frac{1}{\sqrt{2}}(1, -1)$, $R_S^2 = 0$ always and $R_{AS}^2 = \begin{pmatrix} & -\sqrt{2}a_2 i \\ +\sqrt{2}a_2 i & \end{pmatrix}$ below B_c and 0 otherwise (Fig. 3C, middle), where $i = \sqrt{-1}$ to account for the time-reversal symmetry and a_i stands for the Raman scattering strength of the i^{th} mode (see the calculated magnetic field dependence of U_1 and U_2 in SM, Table S4 and S5). This model faithfully reproduces the magnetic field dependence of both 1st-order modes of 2L CrI₃ in LL and RR channels by tuning only λ_i and a_i (Fig. 3D).

Different from 2L CrI₃, N -layer CrI₃ ($N > 2$) undergoes two spin-flip transitions with increasing B_{\perp} , one at $B_{c1} = \pm 0.7$ T for spins in surface layers and the other at $B_{c2} = \pm 1.6$ T for spins in interior layers [1, 2]. For simplicity but without losing any generality, we pick 4L CrI₃ and focus on measurements with the upwards magnetic field and in the RR polarization channel. Figure 4A shows Raman spectra of 1st-order modes taken at $B_{\perp} = 0$ T, 1 T, and 2 T, below B_{c1} , between B_{c1} and B_{c2} , and above B_{c2} , respectively, at 10 K and in the RR channel. At 0 T, we can only reliably resolve three out of 4-fold multiplet of 4L CrI₃, namely, U_1 , U_3 , and U_4 as fitted by the ruby, honey, and royal Lorentzian profiles, respectively. This is because U_2 is spectrally so close to U_1 but has a much weaker intensity (Fig. 1A), thus getting overwhelmed by the strong U_1 in the RR channel. We observe both U_1 and U_4 decrease subsequently at 1 T and 2 T to finite and zero intensity, respectively, whereas U_3 increases at 1 T and then decreases at 2 T. The detailed magnetic field dependence of the U_1 , U_3 , and U_4 integrated intensity is shown in Fig. 4B, displaying the contrasting trends of U_3 to U_1 and U_4 , and those of the 2nd and 3rd-order modes are shown in Fig. 4E and 4F, closely mimicking those of U_1 .

We carry out a similar analysis as we have done for 2L CrI₃ above, but add an additional intermediate magnetic phase $\vec{M} = (1, -1, 1, 1)$ between the layered-AFM of $(1, -1, 1, -1)$ and the fully spin polarized FM of $(1, 1, 1, 1)$. While the structural contribution (R_S^i) is only present for parity-even modes, U_1 and U_3 , and remains magnetic field independent, the layered-magnetism-coupled magnetic contribution (R_{AS}^i) varies proportionally to $\vec{U}_i \cdot \vec{M}$ as \vec{M} changes as a function of B_{\perp} . Figure 4C lists the modes that have finite coupling to every layered magnetic order and

thus nonzero R_{AS}^i , according to which the magnetic contribution of U_1 appears above B_{c1} , that of U_3 emerges between B_{c1} and B_{c2} , and $U_{2,4}$ present below B_{c2} (see the calculated magnetic field dependence of U_1 , U_2 , U_3 , and U_4 in SM, Table S6 and S7). By adjusting λ_i and a_i , the ratio of the magnetic to structural contribution and the overall strength of the i^{th} mode, we successfully show the consistency between the experimental and calculated magnetic field dependence of $U_{1,3,4}$ and predict that of U_2 despite its invisibility in our experiment (Fig. 4D).

In conclusion, we have established the Davydov-splitting of A_g mode of monolayer into N -fold multiplet in N -layer CrI_3 and discovered, distinct from non-magnetic few-layer atomic crystals [24–27], a unique layered-magnetism-assisted phonon scattering mechanism in the magnetic phases of CrI_3 . We find this mechanism extend beyond 1st-order phonons to the multi-phonon modes, and further resolve the distinct magnetic field dependence for different 1st-order modes within the N -fold multiplet in N -layer CrI_3 . Our calculations based on the combination of Davydov-splitting and layered-magnetism-phonon coupling successfully explain the selection rules for individual split modes and capture the rich behavior of their distinct magnetic field dependence, effective for 2D CrI_3 of arbitrary thickness.

Materials and Methods

Sample fabrication CrI_3 single crystals were grown by the chemical vapor transport method, as detailed in Ref. [19]. 1–4L CrI_3 samples were exfoliated in a nitrogen-filled glovebox. Using a polymer-stamping transfer technique inside the glovebox, 1–4L CrI_3 flakes were then sandwiched between two few-layer hBN flakes and transferred onto SiO_2/Si substrates for Raman spectroscopy measurements.

Micro-Raman spectroscopy Micro-Raman spectroscopy measurements were carried out using a 633 nm excitation laser. The incident beam was focused by a $40\times$ objective down to $\sim 3 \mu\text{m}$ in diameter at the sample site, and the power was kept at $80 \mu\text{W}$. The scattered light was collected by the objective in a backscattering geometry, then dispersed by a Horiba LabRAM HR Evolution Raman spectrometer, and finally detected by a thermoelectric cooled CCD camera. A closed-cycle helium cryostat is interfaced with the micro-Raman system for the temperature-dependent measurements. All thermal cycles were performed at a base pressure that is lower than 7×10^{-7} mbar. In addition, a cryogen-free magnet is integrated with the low temperature cryostat for the magnetic field-dependent measurements. In this experiment, the magnetic field was applied along the out-of-plane direction and covered a range of 0 – 2.2 Tesla.

Author contributions

Liuyan Zhao, Rui He, and Wencan Jin conceived the idea and designed the experiment. Zhipeng Ye, Gaihua Ye, and Laura Rojas took the experimental data under the guidance of Liuyan Zhao, Rui He, and Wencan Jin. Wencan Jin, Xiangpeng Luo, Kai Sun, and Liuyan Zhao analyzed the data and performed the calculations of phonon mode split and magnetism-phonon coupling. Bowen Yang, Fangzhou Yin, and Hyun Ho Kim fabricated thin films of CrI_3 under the guidance of Adam W. Tsen. Shangjie Tian, Yang Fu, and Shaohua Yan grew bulk CrI_3 single crystals. Wencan Jin, Xiangpeng Luo, Rui He, and Liuyan Zhao wrote the manuscript.

Acknowledgements

L. Zhao acknowledges support by NSF CAREER Grant No. DMR-1749774. R. He acknowledges support by NSF CAREER Grant No. DMR-1760668 and NSF MRI Grant No. DMR-1337207. A. W. Tsen acknowledges support from the US Army Research Office (W911NF-19-10267), Ontario Early Researcher Award (ER17-13-199), and the National Science and Engineering Research Council of Canada (RGPIN-2017-03815). This research was undertaken thanks in part to funding from the Canada First Research Excellence Fund. K. Sun acknowledges support through NSF Grant No. NSF-EFMA-1741618. H. Lei acknowledges support by the National Key R&D Program of China (Grant No. 2018YFE0202600 and 2016YFA0300504), the National Natural Science Foundation of China (No. 11574394, 11774423, and 11822412), the Fundamental Research Funds for the Central Universities, and the Research Funds of Renmin University of China (18XNLG14, 19XNLG17, and 20XHN062).

-
- [1] D. R. Klein, D. MacNeill, J. L. Lado, D. Soriano, E. Navarro-Moratalla, K. Watanabe, T. Taniguchi, S. Manni, P. Canfield, J. Fernández-Rossier, and P. Jarillo-Herrero, “Probing magnetism in 2D van der Waals crystalline insulators via electron tunneling,” *Science* **360**, 1218–1222 (2018).
- [2] T. Song, X. Cai, M. W.-Y. Tu, X. Zhang, B. Huang, N. P. Wilson, K. L. Seyler, L. Zhu, T. Taniguchi, K. Watanabe, M. A. McGuire, D. H. Cobden, D. Xiao, W. Yao, and X. Xu, “Giant tunneling magnetoresistance in spin-filter van der Waals heterostructures,” *Science* **360**, 1214–1218 (2018).

- [3] H. H. Kim, B. Yang, T. Patel, F. Sfigakis, C. Li, S. Tian, H. Lei, and A. W. Tsen, “One million percent tunnel magnetoresistance in a magnetic van der Waals heterostructure,” *Nano Letters* **18**, 4885–4890 (2018).
- [4] Z. Wang, I. Gutiérrez-Lezama, N. Ubrig, M. Kroner, M. Gibertini, T. Taniguchi, K. Watanabe, A. Imamoğlu, E. Giannini, and A. F. Morpurgo, “Very large tunneling magnetoresistance in layered magnetic semiconductor CrI_3 ,” *Nature Communications* **9**, 2516 (2018).
- [5] B. Huang, G. Clark, E. Navarro-Moratalla, D. R. Klein, R. Cheng, K. L. Seyler, D. Zhong, E. Schmidgall, M. A. McGuire, D. H. Cobden, W. Yao, D. Xiao, P. Jarillo-Herrero, and X. Xu, “Layer-dependent ferromagnetism in a van der Waals crystal down to the monolayer limit,” *Nature* **546**, 270–273 (2017).
- [6] H. H. Kim, B. Yang, S. Li, S. Jiang, C. Jin, Z. Tao, G. Nichols, F. Sfigakis, S. Zhong, C. Li, S. Tian, D. G. Cory, G.-X. Miao, J. Shan, K. F. Mak, H. Lei, K. Sun, L. Zhao, and A. W. Tsen, “Evolution of interlayer and intralayer magnetism in three atomically thin chromium trihalides,” *Proceedings of the National Academy of Sciences* **116**, 11131 (2019).
- [7] S. Li, Z. Ye, X. Luo, G. Ye, H. H. Kim, B. Yang, S. Tian, C. Li, H. Lei, A. W. Tsen, K. Sun, R. He, and L. Zhao, “Magnetic-field-induced quantum phase transitions in a van der Waals magnet,” *Phys. Rev. X* **10**, 011075 (2020).
- [8] B. Huang, G. Clark, D. R. Klein, D. MacNeill, E. Navarro-Moratalla, K. L. Seyler, N. Wilson, M. A. McGuire, D. H. Cobden, D. Xiao, W. Yao, P. Jarillo-Herrero, and X. Xu, “Electrical control of 2D magnetism in bilayer CrI_3 ,” *Nature Nanotechnology* **13**, 544–548 (2018).
- [9] S. Jiang, J. Shan, and K. F. Mak, “Electric-field switching of two-dimensional van der Waals magnets,” *Nature Materials* **17**, 406–410 (2018).
- [10] H. H. Kim, S. Jiang, B. Yang, S. Zhong, S. Tian, C. Li, H. Lei, J. Shan, K. F. Mak, and A. W. Tsen, “Magneto-memristive switching in a 2D layer antiferromagnet,” *Advanced Materials* **32**, 1905433 (2020).
- [11] S. Jiang, L. Li, Z. Wang, K. F. Mak, and J. Shan, “Controlling magnetism in 2D CrI_3 by electrostatic doping,” *Nature Nanotechnology* **13**, 549–553 (2018).
- [12] T. Song, Z. Fei, M. Yankowitz, Z. Lin, Q. Jiang, K. Hwangbo, Q. Zhang, B. Sun, T. Taniguchi, K. Watanabe, M. A. McGuire, D. Graf, T. Cao, J.-H. Chu, D. H. Cobden, C. R. Dean, D. Xiao, and X. Xu, “Switching 2D magnetic states via pressure tuning of layer stacking,” *Nature Materials* **18**, 1298–1302 (2019).

- [13] T. Li, S. Jiang, N. Sivadas, Z. Wang, Y. Xu, D. Weber, J. E. Goldberger, K. Watanabe, T. Taniguchi, C. J. Fennie, K. Fai Mak, and J. Shan, “Pressure-controlled interlayer magnetism in atomically thin CrI_3 ,” *Nature Materials* **18**, 1303–1308 (2019).
- [14] K. L. Seyler, D. Zhong, D. R. Klein, S. Gao, X. Zhang, B. Huang, E. Navarro-Moratalla, L. Yang, D. H. Cobden, M. A. McGuire, W. Yao, D. Xiao, P. Jarillo-Herrero, and X. Xu, “Ligand-field helical luminescence in a 2D ferromagnetic insulator,” *Nature Physics* **14**, 277–281 (2018).
- [15] Z. Sun, Y. Yi, T. Song, G. Clark, B. Huang, Y. Shan, S. Wu, D. Huang, C. Gao, Z. Chen, M. McGuire, T. Cao, D. Xiao, W.-T. Liu, W. Yao, X. Xu, and S. Wu, “Giant nonreciprocal second-harmonic generation from antiferromagnetic bilayer CrI_3 ,” *Nature* **572**, 497–501 (2019).
- [16] B. Huang, J. Cenker, X. Zhang, E. L. Ray, T. Song, T. Taniguchi, K. Watanabe, M. A. McGuire, D. Xiao, and X. Xu, “Tuning inelastic light scattering via symmetry control in the two-dimensional magnet CrI_3 ,” *Nature Nanotechnology* **15**, 212–216 (2020).
- [17] A. McCreary, T. T. Mai, F. G. Utermohlen, J. R. Simpson, K. F. Garrity, X. Feng, D. Shcherbakov, Y. Zhu, J. Hu, D. Weber, K. Watanabe, T. Taniguchi, J. E. Goldberger, Z. Mao, C. N. Lau, Y. Lu, N. Trivedi, R. Valdés Aguilar, and A. R. Hight Walker, “Distinct magneto-Raman signatures of spin-flip phase transitions in CrI_3 ,” *Nature Communications* **11**, 3879 (2020).
- [18] Y. Zhang, X. Wu, B. Lyu, M. Wu, S. Zhao, J. Chen, M. Jia, C. Zhang, L. Wang, X. Wang, Y. Chen, J. Mei, T. Taniguchi, K. Watanabe, H. Yan, Q. Liu, L. Huang, Y. Zhao, and M. Huang, “Magnetic order-induced polarization anomaly of Raman scattering in 2D magnet CrI_3 ,” *Nano Letters* **20**, 729–734 (2020).
- [19] W. Jin, H. H. Kim, Z. Ye, S. Li, P. Rezaie, F. Diaz, S. Siddiq, E. Wauer, B. Yang, C. Li, S. Tian, K. Sun, H. Lei, A. W. Tsen, L. Zhao, and R. He, “Raman fingerprint of two terahertz spin wave branches in a two-dimensional honeycomb Ising ferromagnet,” *Nature Communications* **9**, 5122 (2018).
- [20] D. T. Larson and E. Kaxiras, “Raman spectrum of CrI_3 : An *ab initio* study,” *Physical Review B* **98**, 085406 (2018).
- [21] L. Webster, L. Liang, and J.-A. Yan, “Distinct spin-lattice and spin-phonon interactions in monolayer magnetic CrI_3 ,” *Physical Chemistry Chemical Physics* **20**, 23546–23555 (2018).
- [22] S. Djurdjic-Mijin, A. Šolajić, J. Pešić, M. Šćepanović, Y. Liu, A. Baum, C. Petrovic, N. Lazarević, and Z. Popović, “Lattice dynamics and phase transition in CrI_3 single crystals,” *Physical Review B* **98**, 104307 (2018).
- [23] D. Shcherbakov, P. Stepanov, D. Weber, Y. Wang, J. Hu, Y. Zhu, K. Watanabe, T. Taniguchi, Z. Mao,

- W. Windl, J. Goldberger, M. Bockrath, and C. N. Lau, “Raman spectroscopy, photocatalytic degradation, and stabilization of atomically thin chromium tri-iodide,” *Nano Letters* **18**, 4214–4219 (2018).
- [24] M. Staiger, R. Gillen, N. Scheuschner, O. Ochedowski, F. Kampmann, M. Schleberger, C. Thomsen, and J. Maultzsch, “Splitting of monolayer out-of-plane A_1' Raman mode in few-layer WS_2 ,” *Phys. Rev. B* **91**, 195419 (2015).
- [25] Q. J. Song, Q. H. Tan, X. Zhang, J. B. Wu, B. W. Sheng, Y. Wan, X. Q. Wang, L. Dai, and P. H. Tan, “Physical origin of Davydov splitting and resonant Raman spectroscopy of Davydov components in multilayer $MoTe_2$,” *Phys. Rev. B* **93**, 115409 (2016).
- [26] G. Froehlicher, E. Lorchat, F. Fernique, C. Joshi, A. Molina-Sanchez, L. Wirtz, and S. Berciaud, “Unified description of the optical phonon modes in N-layer $MoTe_2$,” *Nano Letters* **15**, 6481–6489 (2015).
- [27] K. Kim, J.-U. Lee, D. Nam, and H. Cheong, “Davydov splitting and excitonic resonance effects in Raman spectra of few-layer $MoSe_2$,” *ACS Nano* **10**, 8113–8120 (2016).
- [28] Y. Tian, M. J. Gray, H. Ji, R. J. Cava, and K. S. Burch, “Magneto-elastic coupling in a potential ferromagnetic 2D atomic crystal,” *2D Materials* **3**, 025035 (2016).
- [29] P. G. Klemens, “Anharmonic decay of optical phonons,” *Phys. Rev.* **148**, 845–848 (1966).
- [30] R. M. Martin and C. M. Varma, “Cascade theory of inelastic scattering of light,” *Phys. Rev. Lett.* **26**, 1241–1244 (1971).
- [31] R. Merlin, G. Güntherodt, R. Humphreys, M. Cardona, R. Suryanarayanan, and F. Holtzberg, “Multiphonon processes in YbS ,” *Phys. Rev. B* **17**, 4951–4958 (1978).

Figure1

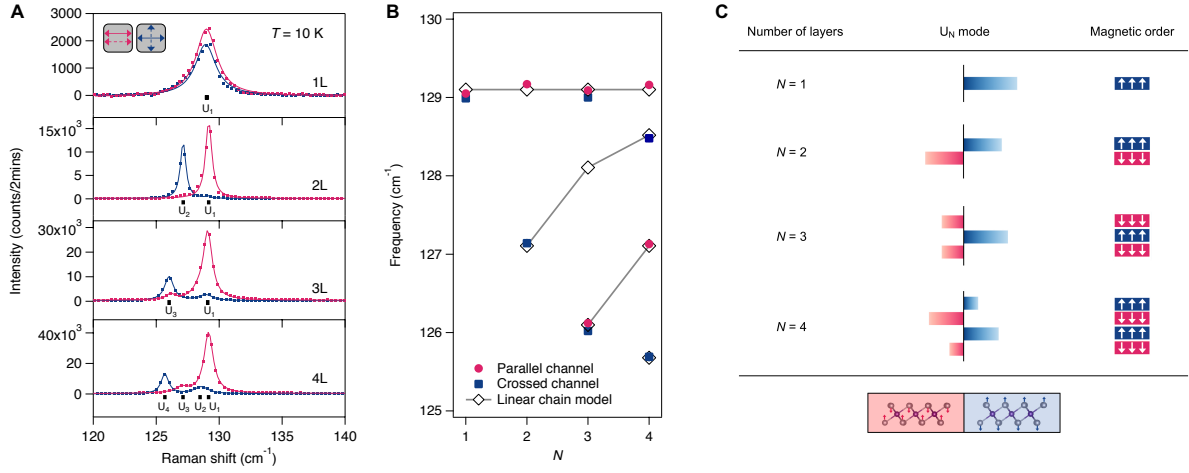


FIG. 1. (A) Raman spectra of 1–4L CrI₃ acquired in linear parallel (ruby) and crossed (royal) channels at 10 K. The solid curves are fits to the raw data (dots). The vertical bars underneath individual spectra denote the fitted frequencies and $U_i (i = 1, 2, \dots, N)$ labels the corresponding modes in N -layer CrI₃. (B) Plot of the fitted frequencies of the modes in (A) as a function of layer number N . Ruby filled circles and royal filled squares correspond to modes extracted from the linear parallel and crossed channels, respectively. Solid curves with open diamonds are fits to the Davydov-split frequencies calculated from the linear chain model. (C) Atomic displacement of the lowest frequency mode U_N along with the layered-AFM order to illustrate that $\vec{U}_i \cdot \vec{M}$ maximized at $i = N$ where \vec{U}_i and \vec{M} share the same parity. The rectangular bar represents the atomic displacement amplitude and phase for individual layers, by its length and color (ruby and royal for opposite phase), respectively.

Figure2

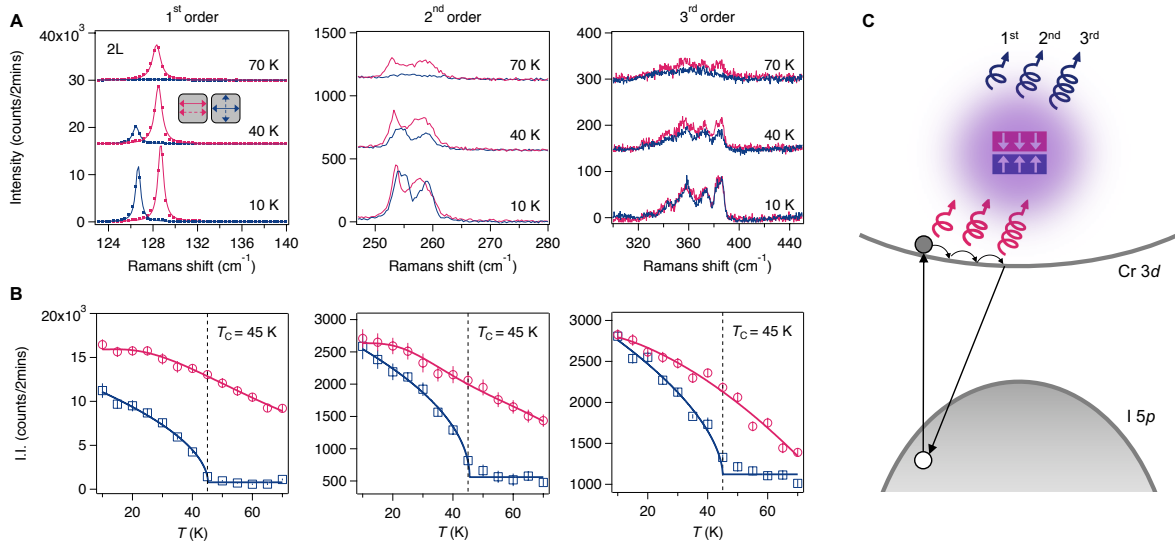


FIG. 2. (A) 1st, 2nd, and 3rd order Raman spectra of 2L CrI₃ in linear parallel (ruby) and crossed (royal) channels at selected temperatures of 70 K, 40 K, and 10 K. Spectra are vertically offset for clarity. 1st order spectra show raw data points and fitting curves, and 2nd and 3rd spectra are raw spectra. (B) Temperature dependence of integrated intensity (I. I.) of 1st, 2nd, and 3rd order Raman modes in the parallel (ruby circles) and crossed (royal squares) channels. Solid curves are fits to the anharmonic decay model in the parallel channel (ruby curves) and the order parameter-like function $I_0 + I\sqrt{T_C - T}$ in the crossed channel (royal curves). Critical temperature $T_C = 45$ K is marked by a dashed vertical line in each panel. (C) Schematic illustration of the cascading process of phonon scattering (ruby) and its layered-AFM assisted counterpart (royal). The springs with one to three windings represent 1st to 3rd order process.

Figure3

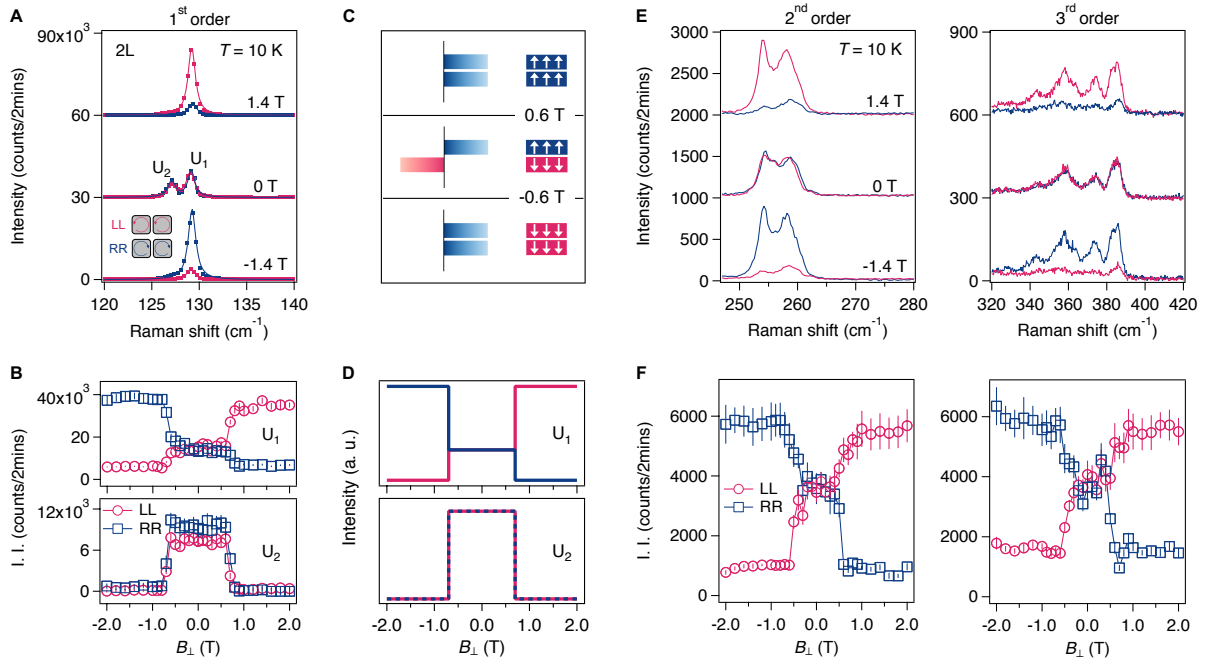


FIG. 3. (A) Raman spectra of 2L CrI₃ in co-circularly polarized channels, LL (ruby) and RR (royal), in selected out-of-plane magnetic field (B_{\perp}) of 1.4 T, 0 T, and -1.4 T. Dots are raw data points and solid curves are fitting curves. (B) Magnetic field dependence of integrated intensity (I. I.) of the two modes of 2L CrI₃, U_1 and U_2 , in both LL (ruby circles) and RR (royal squares) channels. (C) List of phonon modes in 2L CrI₃ that have finite coupling strength $\vec{U}_i \cdot \vec{M}$ for individual magnetic orders that appear at B_{\perp} above and below $B_c = \pm 0.6$ T, the critical magnetic field for the layered-AFM to FM transition. (D) Calculated B_{\perp} dependence of U_1 and U_2 of 2L CrI₃. (E) 2nd and 3rd order Raman modes (raw spectra) acquired in the same condition as (A). (F) B_{\perp} dependence of I. I. of 2nd and 3rd order modes of 2L CrI₃.

Figure4

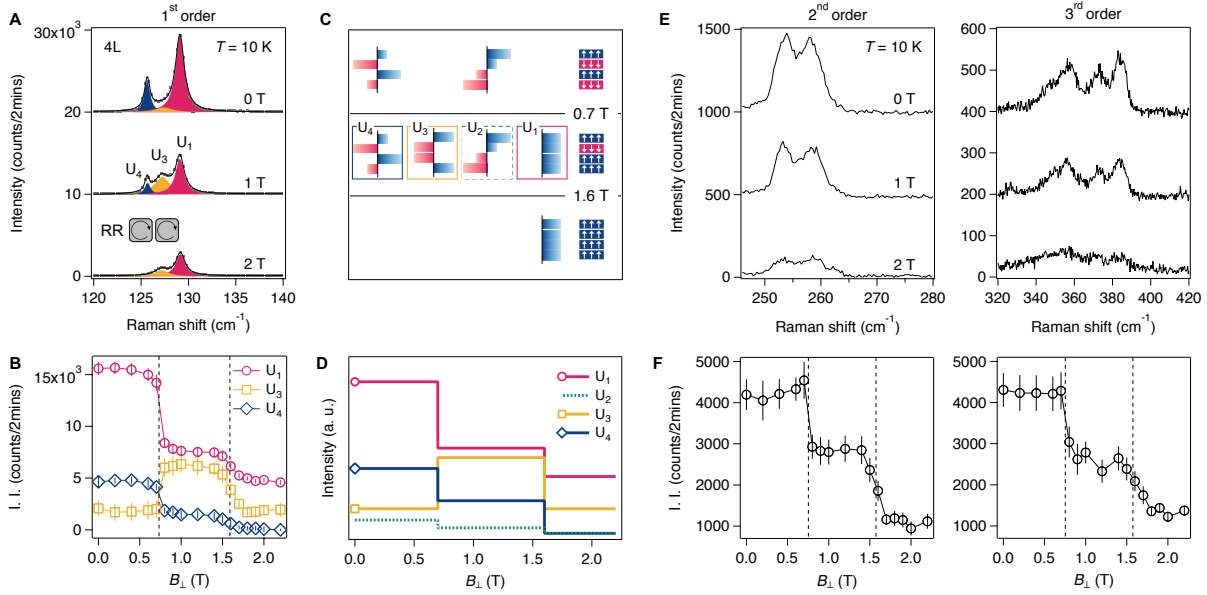


FIG. 4. (A) Raman spectra of 4L CrI₃ in the RR channel in selected B_{\perp} of 0 T, 1 T and 2 T. Grey dots are raw data points and black curves are fits to multiple Lorentzian function. Lorentzian profiles in ruby, honey, and royal correspond to modes U_1 , U_3 , and U_4 of 4L CrI₃. (B) B_{\perp} dependence of I. I. of U_1 (ruby circles), U_3 (honey squares), and U_4 (royal diamonds). Vertical dashed lines mark the critical magnetic fields for spin flip transitions, $B_{c1} = 0.7$ T and $B_{c2} = 1.6$ T. (C) List of phonon modes in 4L CrI₃ that have finite coupling strength $\vec{U}_i \cdot \vec{M}$ for magnetic orders below B_{c1} , between B_{c1} and B_{c2} , and above B_{c2} . Dash emerald box marks U_2 that is not observed in (A) due to its weak intensity and closeness to U_1 . Solid boxes of ruby, honey, and royal color highlight U_1 (ruby), U_3 (honey), and U_4 (royal), respectively. (E) and (F) B_{\perp} dependence of I. I. of 2nd, and 3rd order modes of 4L CrI₃.

Tunable layered-magnetism-assisted rich magneto-Raman effect in a two-dimensional magnet CrI₃

Wencan Jin,^{1,*} Zhipeng Ye,³ Xiangpeng Luo,¹ Bowen Yang,² Gaihua Ye,³ Hyun Ho Kim,^{2,†}
Fangzhou Yin,² Laura Rojas,³ Shangjie Tian,⁴ Hechang Lei,⁴ Adam W. Tsen,² Kai Sun,¹ Rui
He^{3,‡} and Liuyan Zhao,^{1,§}

¹*Department of Physics, University of Michigan, 450 Church Street,
Ann Arbor, Michigan 48109, USA*

²*Institute for Quantum Computing, Department of Chemistry,
and Department of Physics and Astronomy, University of Waterloo,
Waterloo, 200 University Ave W, Ontario N2L 3G1, Canada*

³*Department of Electrical and Computer Engineering, 910 Boston Avenue,
Texas Tech University, Lubbock, Texas 79409, USA*

⁴*Department of Physics and Beijing Key Laboratory of
Opto-electronic Functional Materials & Micro-nano Devices,
Renmin University of China, Beijing 100872 China*

Table of Contents

- I. Full-range Raman spectra for 1–4L CrI₃
- II. Davydov splitting of A_g mode in N-layer CrI₃ described by a linear chain model
- III. Magnetic field dependence of U₂ and U₁ modes in 2L CrI₃
- IV. Magnetic field dependence of U_{1–4} modes in 4L CrI₃

* current affiliation: Department of Physics, Auburn University, 380 Duncan Drive, Auburn, AL 36849, USA

† current affiliation: School of Materials Science and Engineering, Kumoh National Institute of Technology, Gumi,
Gyeongbuk 39177, Korea

‡ rui.he@ttu.edu

§ lyzhao@umich.edu

I. Full-range Raman spectra for 1–4L CrI₃

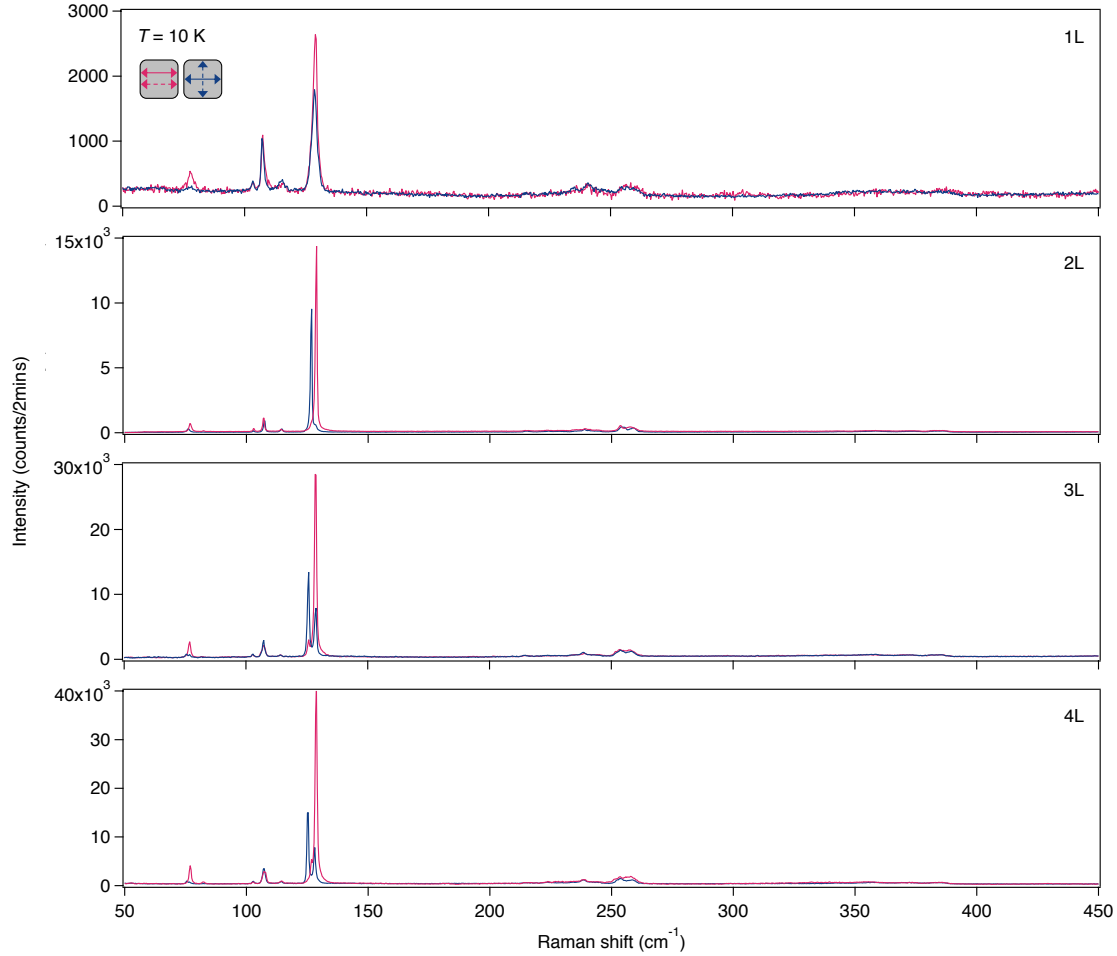


Fig. S1. Full range Raman spectra of 1-4L CrI₃ in the linear parallel and crossed channels acquired at 10 K using 633 nm lasers.

We notice that 1L CrI₃ has a linewidth of $\sim 2.2\text{cm}^{-1}$, clearly broader than those of 2L, 3L, and 4L CrI₃ ($\sim 0.6\text{-}1.0\text{ cm}^{-1}$). Note that in reference Nature Nanotech. 15, 212 (2020) and Nano Letters 20, 729 (2020), a broad linewidth ($\sim 4.0\text{ cm}^{-1}$ and $\sim 3.5\text{ cm}^{-1}$, respectively) for 1L CrI₃ was observed and no explanation has been provided.

We think it may result from a few factors: (a) the ultimate 2D limit of 1L CrI₃ may have stronger fluctuations than its thicker counterparts. (b) the interfacing with hBN flakes on both sides of a CrI₃ flake makes 1L CrI₃ fully in contact with hBN that could cause strong damping effect to phonons. Such an effect is weaker in thicker layers because of their lower surface-to-volume ratio. Or (c) there are simply more defects introduced to 1L CrI₃ as it is much harder to achieve 1L CrI₃

than its thicker counterparts.

The main purpose for using the 633 nm resonant excitation is to enhance the signal level and achieve a good signal to noise ratio. Meanwhile, this resonant excitation does not alter the Raman selection rule. As shown in Fig. S2, Raman spectra taken in both parallel and crossed channels on a same 2L CrI₃ flake with 633 nm and 532 nm excitations exhibit no observable selection rule difference, but a significant enhancement of signal level (by a factor of ~ 50) with the 633 nm laser.

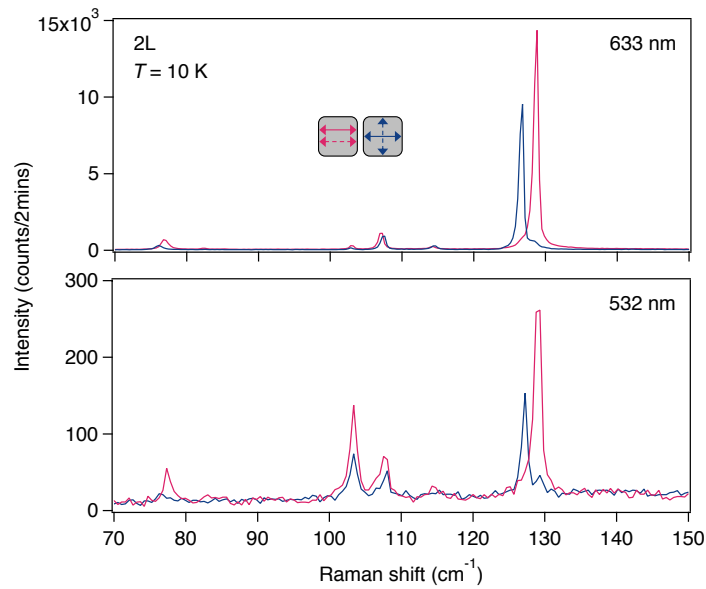


Fig. S2. Raman spectra of 2L CrI₃ in the linear parallel and crossed channels using 633 nm and 532 nm lasers.

II. Davydov splitting of A_g mode in N -layer CrI_3 described by a linear chain model

The Davydov splitting of A_g mode in N -layer CrI_3 can be accounted for by a linear chain model written as

$$H = \sum_{i=1}^N (\frac{1}{2}m\dot{u}_i^2 + \frac{1}{2}k_0u_i^2) + \frac{1}{2}\sum_{i=2}^N k(u_{i-1} - u_i)^2 = \frac{1}{2}U^T KU$$

with eigenmode $U = \begin{pmatrix} u_1 \\ u_2 \\ \vdots \\ u_N \end{pmatrix}$, in which u_i contains both amplitude and phase of the atomic displacement within the i^{th} layer; k_0 and k stand for the force constant of the original A_g mode of monolayer CrI_3 and the coupling constant between adjacent layers, respectively.

We thus obtain a $N \times N$ matrix $K = \begin{pmatrix} k_0+k & -k & 0 & \cdots & \cdots & 0 \\ -k & k_0+2k & -k & & & 0 \\ 0 & -k & k_0+2k & & & 0 \\ \vdots & & & \ddots & & \vdots \\ \vdots & & & & k_0+2k & -k \\ 0 & 0 & 0 & \cdots & -k & k_0+k \end{pmatrix}_{N \times N} = k_0I +$

kG , where I is an identify matrix, and G matrix describes interlayer coupling. Diagonalizing the matrix G gives rise to the N eigenvalues (e_i with $i = 1, 2, \dots, N$) and eigenmodes for N -layer CrI_3 and their parity (see Table S1). We can also obtain the corresponding eigenfrequencies $\Omega(\omega_0, \omega) = \sqrt{\omega_0^2 + e_i \cdot \omega^2}$, with $\omega_0 = \sqrt{\frac{k_0}{m}}$, and $\omega = \sqrt{\frac{k}{m}}$ (see Table S2).

Absence of U_2 mode in the spectrum of 3L CrI_3

As shown in Table S1, U_2 mode of 3L CrI_3 $U_2 = \frac{1}{\sqrt{2}} \begin{pmatrix} 1 \\ 0 \\ -1 \end{pmatrix}$ is parity odd, which is Raman silent in

the parallel channel. Meanwhile, the coupling between U_2 with layered AFM order $M = \begin{pmatrix} 1 \\ -1 \\ 1 \end{pmatrix}$

also vanishes. As a result, it cannot be observed in the crossed channel either. Therefore, U_2 mode is absent in our spectrum of 3L CrI_3 shown in Fig. 1A.






Table. S1. N eigenmodes for N -layer CrI_3 and their parities.

Num. of layers	G Matrix	Eigenvalue	Eigenvector	Parity
$N = 2$	$\begin{pmatrix} 1 & -1 \\ -1 & 1 \end{pmatrix}$	$e_1 = 0$	$U_1 = \frac{1}{\sqrt{2}} \begin{pmatrix} 1 \\ 1 \end{pmatrix}$	even
		$e_2 = -2$	$U_2 = \frac{1}{\sqrt{2}} \begin{pmatrix} 1 \\ -1 \end{pmatrix}$	odd
$N = 3$	$\begin{pmatrix} 1 & -1 & 0 \\ -1 & 2 & -1 \\ 0 & -1 & 1 \end{pmatrix}$	$e_1 = 0$	$U_1 = \frac{1}{\sqrt{3}} \begin{pmatrix} 1 \\ 1 \\ 1 \end{pmatrix}$	even
		$e_2 = -1$	$U_2 = \frac{1}{\sqrt{2}} \begin{pmatrix} 1 \\ 0 \\ -1 \end{pmatrix}$	odd
		$e_3 = -3$	$U_3 = \frac{1}{\sqrt{6}} \begin{pmatrix} 1 \\ -2 \\ 1 \end{pmatrix}$	even
$N = 4$	$\begin{pmatrix} 1 & -1 & 0 & 0 \\ -1 & 2 & -1 & 0 \\ 0 & -1 & 2 & -1 \\ 0 & 0 & -1 & 1 \end{pmatrix}$	$e_1 = 0$	$U_1 = \frac{1}{2} \begin{pmatrix} 1 \\ 1 \\ 1 \\ 1 \end{pmatrix}$	even
		$e_2 = -2 + \sqrt{2}$	$U_2 = \frac{1}{2\sqrt{2 - \sqrt{2}}} \begin{pmatrix} 1 \\ -1 + \sqrt{2} \\ 1 - \sqrt{2} \\ -1 \end{pmatrix}$	odd
		$e_3 = -2$	$U_3 = \frac{1}{2} \begin{pmatrix} 1 \\ -1 \\ -1 \\ 1 \end{pmatrix}$	even
		$e_4 = -2 - \sqrt{2}$	$U_4 = \frac{1}{2\sqrt{2 + \sqrt{2}}} \begin{pmatrix} 1 \\ -1 - \sqrt{2} \\ 1 + \sqrt{2} \\ -1 \end{pmatrix}$	odd

Table. S2. Functional forms of N eigenfrequencies for N -layer CrI_3 .

Num. of layers	Eigenfrequency			
1L	$\Omega_1 = \omega_0$			
2L	$\Omega_1 = \omega_0$	$\Omega_2 = \sqrt{\omega_0^2 - 2\omega^2}$		
3L	$\Omega_1 = \omega_0$	$\Omega_2 = \sqrt{\omega_0^2 - \omega^2}$	$\Omega_3 = \sqrt{\omega_0^2 - 3\omega^2}$	
4L	$\Omega_1 = \omega_0$	$\Omega_2 = \sqrt{\omega_0^2 - (2 - \sqrt{2})\omega^2}$	$\Omega_3 = \sqrt{\omega_0^2 - 2\omega^2}$	$\Omega_4 = \sqrt{\omega_0^2 - (2 + \sqrt{2})\omega^2}$

Table. S3. Computed Raman selection rules and intensities for the layered-AFM state in N -layer CrI_3 .

States		Selection rule	Linear		Circular	
			XX	XY	LL	RR
1L		$\vec{U}_1 \cdot \vec{M} = -1$	a_1^2	$\lambda_1^2 a_1^2$	$(1 - \lambda_1)^2 a_1^2$	$(1 + \lambda_1)^2 a_1^2$
		$\vec{U}_1 \cdot \vec{M} = 1$	a_1^2	$\lambda_1^2 a_1^2$	$(1 + \lambda_1)^2 a_1^2$	$(1 - \lambda_1)^2 a_1^2$
2L		$\vec{U}_1 \cdot \vec{M} = 0$	a_1^2	0	a_1^2	a_1^2
		$\vec{U}_2 \cdot \vec{M} = -\sqrt{2}$	0	$2\lambda_2^2 a_2^2$	$2\lambda_2^2 a_2^2$	$2\lambda_2^2 a_2^2$
		$\vec{U}_1 \cdot \vec{M} = 0$	a_1^2	0	a_1^2	a_1^2
		$\vec{U}_2 \cdot \vec{M} = \sqrt{2}$	0	$2\lambda_2^2 a_2^2$	$2\lambda_2^2 a_2^2$	$2\lambda_2^2 a_2^2$
3L		$\vec{U}_1 \cdot \vec{M} = -0.58$	a_1^2	$0.33\lambda_1^2 a_1^2$	$(1 - 0.58\lambda_1)^2 a_1^2$	$(1 + 0.58\lambda_1)^2 a_1^2$
		$\vec{U}_2 \cdot \vec{M} = 0$	0	0	0	0
		$\vec{U}_3 \cdot \vec{M} = -1.63$	a_3^2	$2.67\lambda_3^2 a_3^2$	$(1 - 1.63\lambda_3)^2 a_3^2$	$(1 + 1.63\lambda_3)^2 a_3^2$
		$\vec{U}_1 \cdot \vec{M} = 0.58$	a_1^2	$0.33\lambda_1^2 a_1^2$	$(1 + 0.58\lambda_1)^2 a_1^2$	$(1 - 0.58\lambda_1)^2 a_1^2$
		$\vec{U}_2 \cdot \vec{M} = 0$	0	0	0	0
		$\vec{U}_3 \cdot \vec{M} = 1.63$	a_3^2	$2.67\lambda_3^2 a_3^2$	$(1 + 1.63\lambda_3)^2 a_3^2$	$(1 - 1.63\lambda_3)^2 a_3^2$
4L		$\vec{U}_1 \cdot \vec{M} = 0$	a_1^2	0	a_1^2	a_1^2
		$\vec{U}_2 \cdot \vec{M} = -0.77$	0	$0.59\lambda_2^2 a_2^2$	$0.59\lambda_2^2 a_2^2$	$0.59\lambda_2^2 a_2^2$
		$\vec{U}_3 \cdot \vec{M} = 0$	a_3^2	0	a_3^2	a_3^2
		$\vec{U}_4 \cdot \vec{M} = -1.85$	0	$3.42\lambda_4^2 a_4^2$	$3.42\lambda_4^2 a_4^2$	$3.42\lambda_4^2 a_4^2$
		$\vec{U}_1 \cdot \vec{M} = 0$	a_1^2	0	a_1^2	a_1^2
		$\vec{U}_2 \cdot \vec{M} = 0.77$	0	$0.59\lambda_2^2 a_2^2$	$0.59\lambda_2^2 a_2^2$	$0.59\lambda_2^2 a_2^2$
		$\vec{U}_3 \cdot \vec{M} = 0$	a_3^2	0	a_3^2	a_3^2
		$\vec{U}_4 \cdot \vec{M} = 1.85$	0	$3.42\lambda_4^2 a_4^2$	$3.42\lambda_4^2 a_4^2$	$3.42\lambda_4^2 a_4^2$

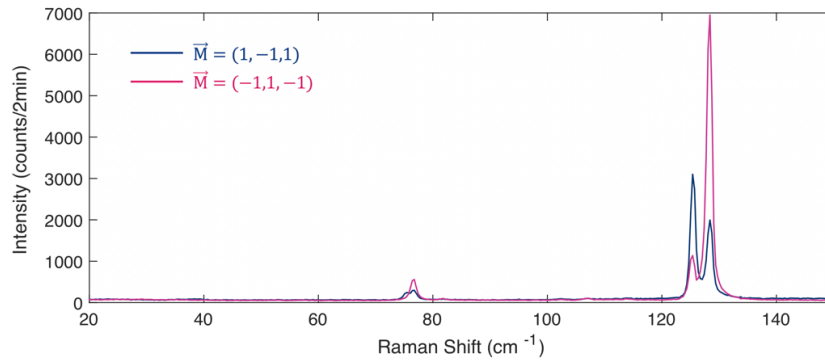


Fig. S3. Raman spectra of 3L CrI_3 in the RR channel for the two time-reversal symmetry related magnetic ground states $\vec{M} = (1, -1, 1)$ and $(-1, 1, -1)$.

III. Magnetic field dependence of U_2 and U_1 modes in 2L CrI_3

Table. S4. Coupling strength ($\vec{U}_i \cdot \vec{M}$) between the phonon mode (\vec{U}_i) with the magnetic order (\vec{M}).

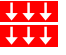
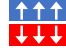









Magnetic order		 $\begin{pmatrix} -1 \\ -1 \end{pmatrix}$	 $\begin{pmatrix} 1 \\ -1 \end{pmatrix}$	 $\begin{pmatrix} 1 \\ 1 \end{pmatrix}$
		Phonon mode		
 $U_2 = \frac{1}{\sqrt{2}} \begin{pmatrix} 1 \\ -1 \end{pmatrix}$	0	$\sqrt{2}$	0	
 $U_1 = \frac{1}{\sqrt{2}} \begin{pmatrix} 1 \\ 1 \end{pmatrix}$	$-\sqrt{2}$	0	$\sqrt{2}$	

Table. S5. Calculated Raman tensor forms and selection rules for the two modes in 2L CrI_3 .

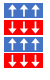











Raman tensor ($R_S^i + \lambda_i R_{AS}^i$)		Selection rule	Linear		Circular	
			XX	XY	LL	RR
U_2	$\vec{U}_2 \cdot \vec{M} = 0$	 $\begin{pmatrix} 0 & 0 \\ 0 & 0 \end{pmatrix}$	0	0	0	0
	$\vec{U}_2 \cdot \vec{M} = \sqrt{2}$	 $\begin{pmatrix} 0 & -\sqrt{2}\lambda_2 a_2 i \\ \sqrt{2}\lambda_2 a_2 i & 0 \end{pmatrix}$	0	$2\lambda_2^2 a_2^2$	$2\lambda_2^2 a_2^2$	$2\lambda_2^2 a_2^2$
	$\vec{U}_2 \cdot \vec{M} = 0$	 $\begin{pmatrix} 0 & 0 \\ 0 & 0 \end{pmatrix}$	0	0	0	0
U_1	$\vec{U}_1 \cdot \vec{M} = \sqrt{2}$	 $\begin{pmatrix} a_1 & -\sqrt{2}\lambda_1 a_1 i \\ \sqrt{2}\lambda_1 a_1 i & a_1 \end{pmatrix}$	a_1^2	$2\lambda_1^2 a_1^2$	$(1 + \sqrt{2}\lambda_1)^2 a_1^2$	$(1 - \sqrt{2}\lambda_1)^2 a_1^2$
	$\vec{U}_1 \cdot \vec{M} = 0$	 $\begin{pmatrix} a_1 & 0 \\ 0 & a_1 \end{pmatrix}$	a_1^2	0	a_1^2	a_1^2
	$\vec{U}_1 \cdot \vec{M} = -\sqrt{2}$	 $\begin{pmatrix} a_1 & \sqrt{2}\lambda_1 a_1 i \\ -\sqrt{2}\lambda_1 a_1 i & a_1 \end{pmatrix}$	a_1^2	$2\lambda_1^2 a_1^2$	$(1 - \sqrt{2}\lambda_1)^2 a_1^2$	$(1 + \sqrt{2}\lambda_1)^2 a_1^2$

IV. Magnetic field dependence of U_{1-4} modes in 4L CrI_3

Table. S6. Coupling strength ($\vec{U}_i \cdot \vec{M}$) between the phonon mode (\vec{U}_i) with the magnetic order (\vec{M}).

Phonon mode	Magnetic order		
	$\begin{pmatrix} 1 \\ -1 \\ 1 \\ -1 \end{pmatrix}$	$\begin{pmatrix} 1 \\ -1 \\ 1 \\ 1 \end{pmatrix}$	$\begin{pmatrix} 1 \\ 1 \\ 1 \\ 1 \end{pmatrix}$
$U_4 = \frac{1}{2\sqrt{2+\sqrt{2}}} \begin{pmatrix} 1 \\ -1-\sqrt{2} \\ 1+\sqrt{2} \\ -1 \end{pmatrix}$	1.85	1.31	0
$U_3 = \frac{1}{2} \begin{pmatrix} 1 \\ -1 \\ -1 \\ 1 \end{pmatrix}$	0	1	0
$U_2 = \frac{1}{2\sqrt{2-\sqrt{2}}} \begin{pmatrix} 1 \\ -1+\sqrt{2} \\ 1-\sqrt{2} \\ -1 \end{pmatrix}$	0.77	-0.54	0
$U_1 = \frac{1}{2} \begin{pmatrix} 1 \\ 1 \\ 1 \\ 1 \end{pmatrix}$	0	1	2

Table. S7. Calculated Raman tensor forms and selection rules for the two modes in 4L CrI₃.

Raman tensor ($R_S^i + \lambda_i R_{AS}^i$)		Selection rule	Linear		Circular	
			XX	XY	LL	RR
U ₄	$\vec{U}_4 \cdot \vec{M} = 1.85$	 $\begin{pmatrix} 0 & -1.85\lambda_4 a_4 i \\ 1.85\lambda_4 a_4 i & 0 \end{pmatrix}$	0	$3.42\lambda_4^2 a_4^2$	$3.42\lambda_4^2 a_4^2$	$3.42\lambda_4^2 a_4^2$
	$\vec{U}_4 \cdot \vec{M} = 1.31$	 $\begin{pmatrix} 0 & -1.31\lambda_4 a_4 i \\ 1.31\lambda_4 a_4 i & 0 \end{pmatrix}$	0	$1.72\lambda_4^2 a_4^2$	$1.72\lambda_4^2 a_4^2$	$1.72\lambda_4^2 a_4^2$
	$\vec{U}_4 \cdot \vec{M} = 0$	 $\begin{pmatrix} 0 & 0 \\ 0 & 0 \end{pmatrix}$	0	0	0	0
U ₃	$\vec{U}_3 \cdot \vec{M} = 0$	 $\begin{pmatrix} a_3 & 0 \\ 0 & a_3 \end{pmatrix}$	a_3^2	0	a_3^2	a_3^2
	$\vec{U}_3 \cdot \vec{M} = 1$	 $\begin{pmatrix} a_3 & -\lambda_3 a_3 i \\ \lambda_3 a_3 i & a_3 \end{pmatrix}$	a_3^2	$\lambda_3^2 a_3^2$	$(1 + \lambda_3)^2 a_3^2$	$(1 - \lambda_3)^2 a_3^2$
	$\vec{U}_3 \cdot \vec{M} = 0$	 $\begin{pmatrix} a_3 & 0 \\ 0 & a_3 \end{pmatrix}$	a_3^2	0	a_3^2	a_3^2
U ₂	$\vec{U}_2 \cdot \vec{M} = 0.77$	 $\begin{pmatrix} 0 & -0.77\lambda_2 a_2 i \\ 0.77\lambda_2 a_2 i & 0 \end{pmatrix}$	0	$0.59\lambda_2^2 a_2^2$	$0.59\lambda_2^2 a_2^2$	$0.59\lambda_2^2 a_2^2$
	$\vec{U}_2 \cdot \vec{M} = -0.54$	 $\begin{pmatrix} 0 & 0.54\lambda_2 a_2 i \\ -0.54\lambda_2 a_2 i & 0 \end{pmatrix}$	0	$0.29\lambda_2^2 a_2^2$	$0.29\lambda_2^2 a_2^2$	$0.29\lambda_2^2 a_2^2$
	$\vec{U}_2 \cdot \vec{M} = 0$	 $\begin{pmatrix} 0 & 0 \\ 0 & 0 \end{pmatrix}$	0	0	0	0
U ₁	$\vec{U}_1 \cdot \vec{M} = 0$	 $\begin{pmatrix} a_1 & 0 \\ 0 & a_1 \end{pmatrix}$	a_1^2	0	a_1^2	a_1^2
	$\vec{U}_1 \cdot \vec{M} = 1$	 $\begin{pmatrix} a_1 & -\lambda_1 a_1 i \\ \lambda_1 a_1 i & a_1 \end{pmatrix}$	a_1^2	$\lambda_1^2 a_1^2$	$(1 + \lambda_1)^2 a_1^2$	$(1 - \lambda_1)^2 a_1^2$
	$\vec{U}_1 \cdot \vec{M} = 2$	 $\begin{pmatrix} a_1 & -2\lambda_1 a_1 i \\ 2\lambda_1 a_1 i & a_1 \end{pmatrix}$	a_1^2	$4\lambda_1^2 a_1^2$	$(1 + 2\lambda_1)^2 a_1^2$	$(1 - 2\lambda_1)^2 a_1^2$